LA-UR-15-27981
Approved for public release; distribution is unlimited.

Title: Thermal transport in UO2 with defects and fission products by molecular dynamics simulations

Author(s): Liu, Xiang-Yang
Cooper, Michael William Donald
Mcclellan, Kenneth James
Lashley, Jason Charles
Byler, Darrin David
Stanek, Christopher Richard
Andersson, Anders David Ragnar

Intended for: Report

Issued: 2015-10-14

Thermal transport in UO_2 with defects and fission products by molecular dynamics simulations

X.-Y. Liu[a], M. W. D. Cooper[a], K. McClellan[a], J. Lashley[a], D. Byler[a], C. R. Stanek[a], D. A. Andersson[a]

[a]*Materials Science and Technology Division, Los Alamos National Laboratory P.O. Box 1663, Los Alamos, NM 87545*

Abstract

The importance of the thermal transport in nuclear fuel has motived a wide range of experimental and modelling studies. In this report, the reduction of thermal transport in UO_2 due to defects and fission products has been investigated using non-equilibrium MD simulations, with two sets of empirical potentials for studying the degregation of UO_2 thermal conductivity including a Buckingham type interatomic potential and a recently developed EAM type interatomic potential. Additional parameters for U^{5+} and Zr^{4+} in UO_2 have been developed for the EAM potential. The thermal conductivity results from MD simualtions are then corrected for the spin-phonon scattering through Callaway model formulations. To validate the modelling results, comparison was made with experimental measurements on single crystal hyper-stoichiometric UO_{2+x} samples.

1. Introduction

The thermal conductivity of UO_2 is an important property in nuclear reactor design and safety [1]. It affects the fuel performance since it governs thermal transport from the fuel to the coolant. The temperature distribution in fuel affects thermal expansion, fission gas release and mechanical properties amongst others. During operation nuclear fuels are subject to a number of processes that degrade thermal conductivity, such as radiation damage, transmutation or the generation of fission products, point defects and microstructural features.

The importance of the thermal conductivity of nuclear fuel has motivated a wide range of experimental and modelling studies. Primarily the thermal conductivity as function of burnup has been clearly quantified by reviewing large numbers of experimental studies [2, 3]. However, in order to evaluate fuel performance beyond conventional reactor conditions and burnup limits one must have a detailed understanding of the underlying mechanisms for thermal conductivity degradation. Atomistic simulations, thus, make an important contribution when deconvoluting the role of different processes in thermal conductivity degradation. These studies include thermal transport in bulk UO_2 [1, 4–6], non-stoichiometric $UO_{2\pm x}$ [7–9], intrinsic defects [5, 9], grain-boundary effects [10], dislocations [11] and pores or bubbles [12]. Additionally, these effects have also been studied in mixed oxide fuels [13–15].

In recent work, the role of UO_2 magnetism in phonon scattering has been investigated experimentally [1]. It demonstrates that, particularly at lower temperatures, UO_2 thermal conductivity is greatly limited by spin-phonon scattering enabled by dynamic splitting the cubic groundstate of the uranium ions. Although attempts are being made to develop magnetic molecular dynamics (MD) methods [16], spin dynamics cannot currently be captured by MD simulations. Nonetheless parameters for magnetic scattering can be explicitly derived by fitting the Callaway model to experimental data. Subsequently, these magnetic terms can be combined with results from pure MD to demonstrate the extent to which spin-phonon scattering accounts for the mismatch between experiment and modelling.

In this work, Callaway model parameters are determined from molecular dynamics (without spin-phonon scattering) for the UO_2 lattice containing intrinsic defects and the fission products Zr, La and Xe. The Callaway model parameters for these defective structures can be combined with the magnetic terms derived from very low temperature ex-

periments to give accurate predictions of the degradation of UO_2 thermal conductivity. Two sets of empirical potentials are used in this study: i) a Buckingham potential [17] developed by Busker *et al.* [18] and ii) a potential recently developed by Cooper *et al.* [19] that includes many-body effects through the embedded atom method (EAM) [20] combined with Buckingham-Morse pairwise interactions [17, 21]. These results will be used to develop enhanced continuum thermal conductivity models for MARMOT and BISON with INL [22].

In order to validate the modelling results, comparison was made with experimental measurements on single crystal hyper-stoichiometric UO_{2+x} samples to establish the extent of defect scattering for interstitial oxygen ions and U^{5+} cations. The measurements were performed from 4 K to 300 K, enabling phonon-phonon, defect-phonon and spin-phonon scattering contributions to be separated. Comparison is also made with higher temperature literature data for further validation and to avoid complications of UO_2–U_4O_9 phase transitions occuring at high temperatures.

2. Methods

2.1. Non-equilibrium MD simulations

In non-metallic solids, phonons dominate thermal transport. This provides the basis of the MD based methodology to predict the thermal conductivity of these materials. Here, we have employed the non-equilibrium MD method, which is often referred to as the "direct method" [23–25]. In this method, a heat current (J) is applied to the system, and the thermal conductivity κ is computed from the time-averaged temperature gradient from Fourier's law,

$$\kappa = -\frac{J}{\partial T/\partial z} \tag{1}$$

A supercell containing $n_1 \times n_2 \times n_3$ cubic unit cells of UO_2 is constructed. Periodic boundaries are applied in all three dimensions. The heat flow is in the z direction. There are 1 nm thick cold and hot slabs defined at $z = 0$ and $z = L_z/2$ from which heat is removed or added during the simulations. L_z is the periodic length of the supercell in the z direction. For all MD simulations using the Buckingham type potential, n_1 and n_2 are set to 3 while for all MD simulations using the EAM type potential, n_1 and n_2 are set to 4. The choice of the above settings is based on the cutoff distance used in the interatomic potentials. The dependence of the computed thermal conductivity on cross sectional area has been shown to be weak [26].

In this work, the thermal conductivity calculations were carried out with the direct method as implemented in LAMMPS package [27]. The system is equilibrated initially for 50 ps in the NVT (constant number, constant volume, and constant temperature) ensemble at the desired temperature, followed by another 50 ps in the NVE (constant number, constant volume, and constant energy) ensemble. Subsequently, non-equilibrium MD runs were applied to the system, for a period of 10 - 26 ns, the first 5 ns of which was used to accommodate the transient behavior. After that, the temperature profiles were averaged over the rest of the MD time.

There are two types of heat control methods in LAMMPS. One is based on the Muller-Plathe algorithm [24]. In this algorithm, the energy swap between the hottest particle in the cold region and the coldest atom in the hot region is used to remove or add heat to the corresponding regions. By controlling the frequency of swaps during MD, the heat flux between the hot and the cold regions is controlled at the desired level. Alternatively, the method of Jund and Jullien [23] can be used. In this scheme, a fixed amount of energy (ΔE) is added or subtracted from the hot and cold region by velocity rescaling every time step while preserving the total momentum of the atoms in the region, so that

$$V_i^{\vec{new}} = \vec{V_i} + (1-\alpha)\frac{\vec{P}}{\sum m_i} \tag{2}$$

$$\alpha = \sqrt{1 \pm \frac{\Delta E}{E_k - 0.5\sum m_i V_G^2}} \tag{3}$$

where V_G is the center of mass velocity, $V_G = |\vec{P}|/\sum m_i$.

The original Jund and Jullien algorithm was derived for single species system. We found that it applies to systems with multiple species as well. Another constant heat flux algorithm using velocity rescaling from Ikeshoji and Hafskjold [25], which was originally derived for multiple species system is also widely used. These two algorithms are not equivalent, reflecting different flavors in the formulation since the mathematical solution of constant energy change while preserving momentum in a given region is not unique. We found that precise

control of the heat flux is important for studying the length dependence of the thermal conductivity. However, the control of the heat flux by using Muller-Plathe algorithm for given swap frequency is not good since the result depends on other simulation conditions. For this reason, the method of Jund and Jullien is adopted in all our MD simulations. The heat flux used in the simulations is 0.001/A - 0.002/A eV/nm^2 per time step, where A is the cross section area of the simulation cell.

To fit the temperature profiles, a least-squares fit for the linear regression is used. The temperature profiles were fitted in the ranges w < z < L_z/2 - w, and L_z/2 + w < z < L_z - w, with the choice of the excluded width w as 0.13L_z, in agreement with earlier studies [28]. The obtained gradients from left and right slopes in the temperature profiles are then averaged to determine the thermal conductivity.

In the MD simulations, a fairly significant portion of phonons propagate ballistically through the system due to the large phonon mean free path relative to the simulation supercells. However, scattering due to the hot and cold regions limits the thermal conductivity, particularly at low temperatures. Thus, the thermal conductivity is greater for longer supercells that increase the separation between the hot and cold regions. There is a linear relationship between the inverse of thermal conductivity and the inverse of supercell length that can be extrapolated to determine bulk thermal conductivity, as is describer previously [1]. L_z is varied from 19 to 76 nm, enabling the extrapolation to be made.

2.2. Interatomic potentials

Two sets of empirical potentials are used as basis for studying the degredation of UO_2 thermal conductivity due to defects and fission products: i) the Buckingham potential by Busker *et al.* [18] and ii) the combined Buckingham-Morse and EAM potential developed by Cooper *et al.* [19]. The Buckingham potentials are classical potentials that describe the ionic solids well, and have been constructed to describe UO_2. The advantage of the Busker potential is the availability of large parameter set with the ability to describe several fission products in UO_2. The previously reported parameters are used here to describe the U^{4+}-O^{2-} [18], O^{2-}-O^{2-} [29] interactions in UO_2, as well as the Xe^0-U^{4+} [30] , Xe^0-O^{2-} [31] , La^{3+}-O^{2-} [32] , Zr^{4+}-O^{2-} [32], fission product interactions with UO_2. For U^{3+} and U^{5+} charge compensation of defects in UO_2, the U^{3+}-O^{2-} [33], U^{5+}-O^{2-} [34] interactions developed in literature are used.

The advantage of the potential developed by Cooper *et al.* [19] is ability to accurately reproduce a broad range of thermophysical properties of UO_2, such as the thermal expansion, specific heat and the elastic constants from 300 K to 3000 K. It also reproduces the UO_2 melting point. Although UO_2 and La^{3+}-O^{2-} interactions have been reported in the literature, it was necessary to develop new parameter sets for the U^{5+} and Zr^{4+} species in this work (see section 3). This set of potential provides a possibility to model the thermal behaviors of UO_2 in an accurately manner, based on the relevant properties well fitted.

For computational efficiency, the Wolf summation [35] is used to compute the long-range Coulombic interactions.

2.3. The Callaway model fitting procedure

According to the Callaway model [36], whick assumes a Debye phonon spectrum, the thermal conductivity, k, above the Néel temperature can be expressed in terms of speed of sound, v, the phonon relaxation time, τ_p, the phonon frequency, ω, and the temperature, T:

$$k = \frac{k_B}{2\pi v}\left(\frac{k_B T}{\hbar}\right)\int_0^{\Theta_D/T}\frac{\tau_p x^4 e^x}{(e^x-1)^2}dx \qquad (4)$$
$$x = \hbar\omega/k_B T$$

where $\hbar$, Θ_D and k_B represent the reduced Plank constant, the Debye temperature and the Boltzmann constant respectively.

The relaxation time is governed by various scattering processes that act to limit thermal conductivity. Typically included are point defect scattering (D), boundary scattering (B) and Umpklapp processes (U), although in UO_2 it is also necessary to include spin scattering (S) [1] as an extension to the standard Callaway Model. The inverse relaxation times can be combined according to the Matthiessens's relaxation rule such that $\tau_p^{-1} = \tau_D^{-1} + \tau_B^{-1} + \tau_U^{-1} + \tau_S^{-1}$, whereby the separate

contributions are defined as:

$$\tau_D^{-1} = Dx^4T^4 = D\left(\frac{\hbar\omega}{k_B}\right)^4 \quad (5)$$

$$\tau_B^{-1} = B \quad (6)$$

$$\tau_U^{-1} = UT^3x^2e^{-\Theta_D/bT} = UT\left(\frac{\hbar\omega}{k_B}\right)^2 e^{-\Theta_D/bT} \quad (7)$$

$$\tau_s^{-1} = \sum_i \frac{C_i\omega^4}{(\omega^2-\omega_{S,i})}F_i(T) \quad (8)$$

The additional spin scattering expression for τ_S^{-1} contains the resonance frequency, $\omega_{S,i}$, the phonon-spin coupling constant, C_i, and $F_i(T)$ contains information about the two-level system ($i = 1, 2$). Fitting of D, B, U, b, C_1, C_2, $\hbar\omega_{S,1}$ and $\hbar\omega_{S,2}$ to experimental data has previously been conducted by Gofryk *et al.* [1] and are reported in Table 1 for the 110 direction.

The defect (D), boundary (B), Umpklapp (U, b) parameters make up the classical phonon scattering components of thermal conductivity, which can be fitted to the results of MD. However spin scattering, being excluded from MD, can be subsequently introduced through the Callaway model using the experimentally determined parameters reported in Table 1. The approach used in this work can be summarised as such: i) initially D, B, U and b are all fitted to the MD results for pure UO_2 (with spin scattering excluded from the model) then ii) the experimentally determined C_1, C_2, $\omega_{S,1}$ and $\omega_{S,2}$ from Table 1 are reintroduced. This provide a version of the Callaway model for pure UO_2 that incorporates MD determined classical contributions with the experimental magnetic effects and accounts for significant discrepancies between modelling and experiment. Subsequently, it is possible to refit only the defect scattering term (D) to MD data for the defective UO_2 lattice (B, U and b are maintained from the pure UO_2 fitting). Again by reintroducing the experimental spin scattering parameters an accurate description of the degradation of thermal conductivity due to defect accumulation is obtained. Any coupling between spin and defects are ignored, as defect concentrations investigated here are assumed to be low enough not to influence UO_2 magnetism.

3. Fitting ZrO_2 EAM potential

3.1. Fitting procedure

Like previous centrosymmetric potentials, such as pair potentials [37], the EAM potential form (developed previously for actinide oxides [19]) could not stabilise the monoclinic ZrO_2 crystal structure. Therefore, fitting was carried out to the tetragonal elastic constants from DFT and the tetragonal experimental lattice parameters [38–40].

- Elastic constants predicted by the potential from energy minimisation in GULP [41] were fitted to the DFT elastic constants.
- The temperature dependence of the tetragonal ZrO_2 lattice constants predicted by the potential in MD using LAMMPS [27] were fitted to the room temperature data of Bondars *et al.* [38] and high temperature XRD data from Aldebert and Traverse [39] and Teufer [40].

At each iteration of the fitting procedure the tetragonal ZrO_2 structure was equilibrated at 300 K and 1600 K for 20 ps with the lattice parameters averaged over the final 10 ps. Simultaneously, the 0 K elastic constants were determined using GULP. By comparison to the experimental lattice parameters at the relevant temperature and the DFT elastic constants the potential parameters were iteratively refined to improve the match.

So that consistency was maintained with the previous actinide oxide potential set, the O^{2-}-O^{2-} parameters were fixed at their previous values and the partial charges are proportional to their formal values such that $q_\alpha = Z_\alpha^{eff}|e|$, where $Z_{Zr}^{eff} = 2.2208$. This consistency enabled the degradation of UO_2 thermal conductivity due to Zr_U substitutional defects to be investigated. Additionally, the mixed cation U^{4+}-Zr^{4+} interactions were defined in similar terms to previous mixed cation parameters [42], such that $A_{U^{4+}Zr^{4+}} = 18600$ and $\rho_{Zr^{4+}Zr^{4+}}$ is scaled to cation radii [43]. Subsequently, $\rho_{U^{4+}Zr^{4+}}$ is determined from $\rho_{Zr^{4+}Zr^{4+}}$ and $\rho_{U^{4+}U^{4+}}$ by using equation 9:

$$\rho_{\alpha\beta} = (\rho_{\alpha\alpha}.\rho_{\beta\beta})^{\frac{1}{2}} \quad (9)$$

The final parameter set derived by the fitting process is summarised in Table 2.

3.2. Comparison with DFT

Tables 3 and 4 report the elastic constants and lattice parameters predicted by the new EAM potential. The DFT predictions used in fitting are included for comparison. A reasonable agreement is

Table 1: Callaway model parameters from Gofryk *et al.* [1] that were fitted to experimental thermal conductivity in the 110 direction.

Defect, boundary and Umpklapp terms			
D ($K^{-4}s^{-1}$)	B (s^{-1})	U ($K^{-3}s^{-1}$)	b
267.79038	2.422×10^8	31507.656	2.1664834
Spin Scattering terms			
C_1 (s^{-1})	C_2 (s^{-1})	$\hbar\omega_{S,1}$ (eV)	$\hbar\omega_{S,2}$ (eV)
1.120×10^-12	2.669×10^-12	0.0035252	0.0034292

Table 2: Potential parameters for ZrO_2 using the same potential form reported previously [19]. O-O parameters are also unchanged from the previous work.

Pair Parameters			
	Zr^{4+}-U^{4+}	Zr^{4+}-Zr^{4+}	Zr^{4+}-O^{2-}
$A_{\alpha\beta}$ (eV)	18600	18600	1147.471
$\rho_{\alpha\beta}$ (Å)	0.25172	0.23066	0.32235
$C_{\alpha\beta}$ (eV.Å^6)	0.0	0.0	0.0
$D_{\alpha\beta}$ (eV)	-	-	1.2269
$\gamma_{\alpha\beta}$ (Å^{-1})	-	-	1.4482
$r^0_{\alpha\beta}$ (Å)	-	-	1.998
EAM Parameters			
G_{Zr} (eV.Å$^{1.5}$)	1.597		
n_{Zr} (Å^5)	1188.786		

achieved for all single crystal elastic constants with the exception of C_{33}. However, this relates to strain in line with the c lattice parameter, which as can be seen in Table 4 is significantly over estimated by DFT compared to the experimental data used to fit the potential. It is important to note that fitting was not done to the DFT lattice parameters.

Comparison with a range of DFT data from literature shows good agreement with the potential for all single crystal elastic constants. Furthermore, the lattice constants lie within the range of DFT values and the agreement with the experimental data is also very good.

Although not used in the fitting procedure, the experimental values for the elastic constants of Ce-doped ZrO_2 by Kisi and Howard [44] are also included in Table 3, however, it is not clear to what extend Ce-doping alters the elastic constants.

3.3. Comparison with experimental thermal expansion

Figure 1 shows thermal expansion of the a and b lattice parameters as predicted using the new potential; there is a good agreement with the experimental value over a wide range of temperatures. Similarly, the agreement for lattice parameter c is also good (see Figure 2).

The sudden change in behaviour at ≈2000 K in Figures 1 and 2 seems to indicate a phase transition. If this is due to the high temperature fluorite phase of ZrO_2 (lattice parameter = a_{cubic}) then the following relationship should be true:

$$a_{cubic} = c = \sqrt{a^2 + b^2} = a\sqrt{2}$$
$$\frac{a}{c} = \frac{\sqrt{2}}{2} = 0.7071 \quad (10)$$

It can be seen in Figure 3 that the tetragonal to fluorite phase change occurs at 2000 K. This is a long way off the value of 2650 K shown in the phase diagram [51]. Nonetheless, the previous potential of Schelling *et al.* [37] also exhibits a phase transition at 2000 K. Additionally, tt should be noted that in Figure 3 the experimental results seem to indicate that phase transition is beginning to occur below the temperature given in the phase diagram [51].

4. Fitting UO_{2+x}

Under hyper-stoichiometric UO_{2+x} conditions U^{4+} becomes oxidised to U^{5+}. It is, therefore, necessary to derive suitable parameters for the description of U^{5+}-O^{2-}, U^{5+}-U^{4+} and U^{5+}-U^{5+} interactions. For the cation-cation interactions the covalent Morse term was omitted, as was the dispersive interaction within the Buckingham term. The remaining A and ρ Buckingham parameters for the U^{5+}-U^{5+} interactions were determined in a similar fashion to previous cation terms [42]. As such, $A_{U^{5+}U^{5+}}$ was fixed at 18600 eV and $\rho_{U^{5+}U^{5+}}$ was scaled to the U^{5+} ionic radius [43] giving 0.24287. Subsequently the mixed cation $\rho_{U^{5+}U^{4+}}$ was determined using equation 9. The manybody EAM parameters for U^{5+} remain unchanged from the U^{4+} case.

The U^{5+}-O^{2-} pair interactions were fitted to the DFT structure for bcc U_4O_9 reported previously by Andersson *et al.* [52] by adjusting the relevant

Table 3: Elastic constants predicted by the potential alongside the DFT values used in fitting. Additional DFT data and experimental results for Ce-doped ZrO_2 are included for comparison.

	Fitting Data		Validation Data	
(GPa)	EAM Potential	DFT (present study)	DFT [45–48]	Exp. (Ce-doped) [44]
C_{11}	338	334.25	293 - 401	327
C_{33}	313	251	248 - 385	264
C_{44}	41.7	9.37	9.08 - 51.0	59
C_{66}	166	153	152 - 187	64
C_{12}	229	207	211 - 248	100
C_{13}	94.2	48.9	51.9 - 111	62

Table 4: Static lattice constants and comparison with DFT data used in fitting.

	Fitting Data		Validation Data	
(Å)	EAM Potential	DFT (present study)	DFT [45–48]	Exp. [49, 50]
a	3.60	3.62	3.27-3.61	3.59-3.60
c	5.19	5.28	5.14-5.28	5.18

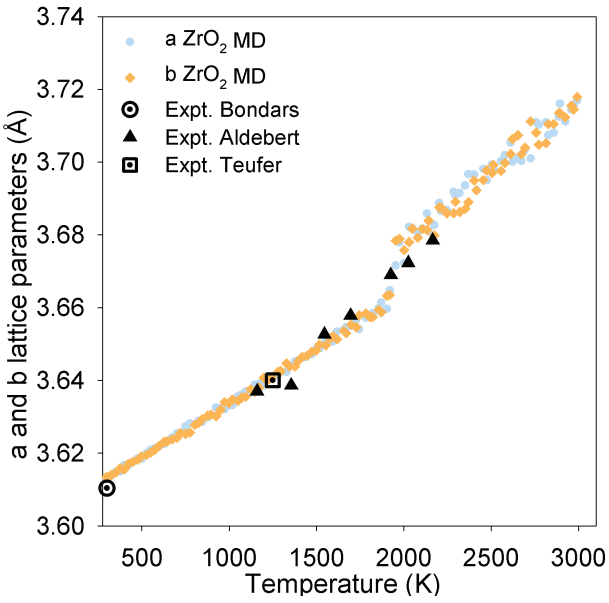

Figure 1: The variation of the a and b lattice parameters of tetragonal ZrO_2 as a function of temperature using the new potential with comparison to experimental data [38–40].

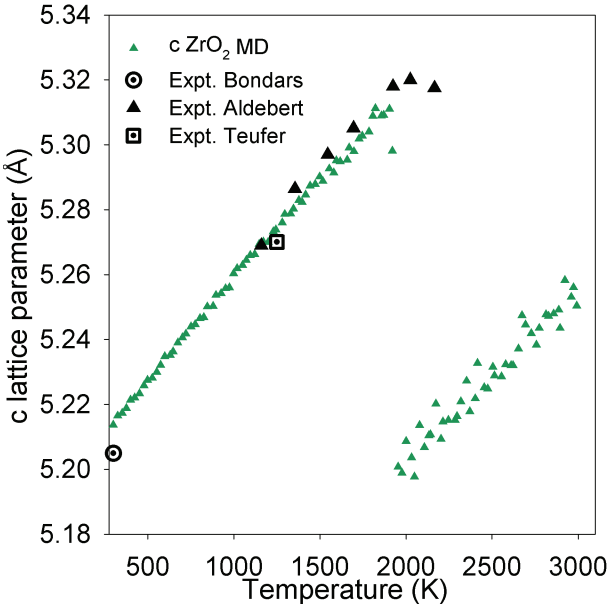

Figure 2: The variation of the c lattice parameter of tetragonal ZrO_2 as a function of temperature using the new potential with comparison to experimental data [38–40].

potential parameters in order to minimise the interatomic forces for that structure. The DFT structure calculated by Andersson *et al.* [52] is shown in Figure 4a with U^{5+} ions highlighted in blue. External pressure on the supercell was omitted from fitting as disagreement between the DFT and empirical potential lattice parameter for UO_2 makes this unreliable. Therefore, fitting was simultaneously carried out to the experimental change in lattice parameter as a function of hyper-stoichiometry, x, by equilibrating five 5×5×5 $UO_{2.1}$ fluorite supercells at 300 K over 20 ps and determining the lattice parameter over the final 10 ps (O_i and U^{5+} cations were randomly distributed throughout the lattice).

The final parameter set for U^{5+} derived by the fitting process is summarised in Table 5. Similarly to ZrO_2 potential fitting, the O^{2-}-O^{2-} parameters are unchanged and $Z^{eff}_{U^{5+}} = 2.7760$.

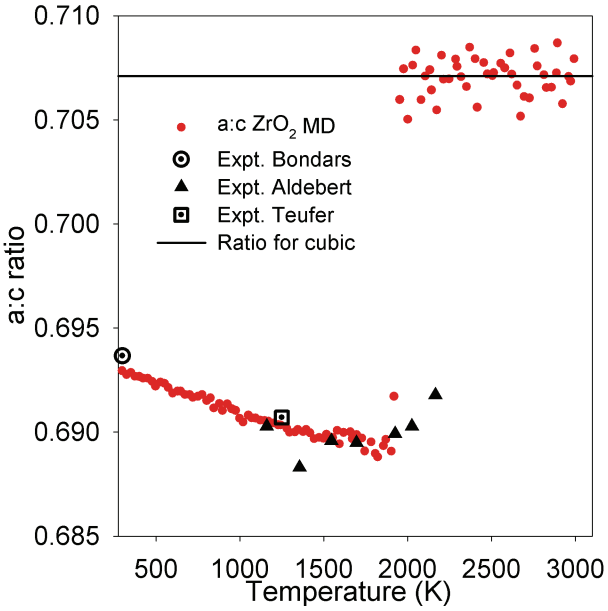

Figure 3: The variation of the a:c ratio of tetragonal ZrO_2 as a function of temperature using the new potential with comparison to experimental data [38–40]. When $\frac{a}{c} = 0.7071$ the tetragonal structure has changed to the fluorite structure (i.e. above 2000 K).

4.1. Comparison with fitting data

Although the atomic forces were not completely minimised during fitting the average atomic force is 0.147 eV·Å^{-1} when using the parameter set in Table 5 in conjunction with the DFT structure [52] shown in Figure 4a. This represents a reasonable agreement with the fitting data. However, the maximum force on a single atom was 2.78 eV·Å^{-1} indicating that some atoms will move noticeably during relaxation. The fully relaxed structure predicted by the new potential is shown in Figure 4b, thus confirming differences compared to the predicted DFT structure. However, this is not unexpected due to the far more complex interactions of a DFT calculation.

Figure 5 shows a good agreement with the change in experimental lattice parameter, a, as a function of hyper-stoichiometry, x, for UO_{2+x}. This is shown by the close agreement in the slope $\frac{da}{dx}$ (also included in Figure 5) and indicates that the new potential provides an accurate description of the U^{5+} defect volume.

Table 5: Potential parameters for U^{5+} using the same potential form reported previously [19]. U^{4+}-O^{2-}, U^{4+}-U^{4+} and O^{2-}-O^{2-} parameters are kept the same as for the previous actinide oxide potential set [19].

Pair Parameters			
	U^{5+}-U^{4+}	U^{5+}-U^{5+}	U^{5+}-O^{2-}
$A_{\alpha\beta}$ (eV)	18600	18600	1155.631
$\rho_{\alpha\beta}$ (Å)	0.25829	0.24287	0.34648
$C_{\alpha\beta}$ (eV.Å^6)	0.0	0.0	0.0
$D_{\alpha\beta}$ (eV)	-	-	1.9317
$\gamma_{\alpha\beta}$ (Å^{-1})	-	-	1.4881
$r^0_{\alpha\beta}$ (Å)	-	-	2.0709
EAM Parameters			
$G_{U^{5+}}$ (eV.Å$^{1.5}$)	1.806		
$n_{U^{5+}}$ (Å^5)	3450.995		

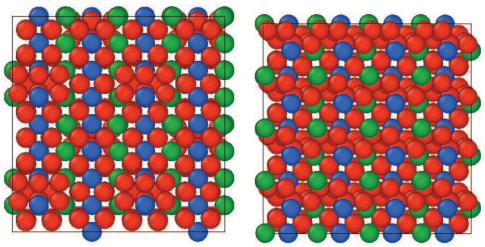

Figure 4: The structures for the U_4O_9 bcc structure predicted by a) DFT [52] and b) the new potential (Table 5). U^{5+}, U^{4+} and O^{2-} ions are indicated by blue, green and red spheres respectively.

5. Results

5.1. Pure UO_2

In figure 6a, the MD simulation results employing the Buckingham potentials developed by Busker et al are shown, with the thermal conductivities κ for pure UO_2 at different temperatures (300-1500 K). As expected, the κ values decrease when T increases. Clearly, as shown in figure 6a, the κ values are substantially higher than the experimental values by Fink et al. The MD values are fitted to the Callaway model initially and was described well, as shown in figure 6a. After being corrected for the magnetic UO_2 scattering contributions as described in the Methods section, the κ values are greatly reduced, especially at low temperature region. The corrected values of κ are closer to the experimental data, albeit there are still some differences, which can most likely be attributed to uncertainties or inaccuracies of the force-field description in the MD potential. Thus, the magnetic correction does have a substantial improvement compared to the experimental values.

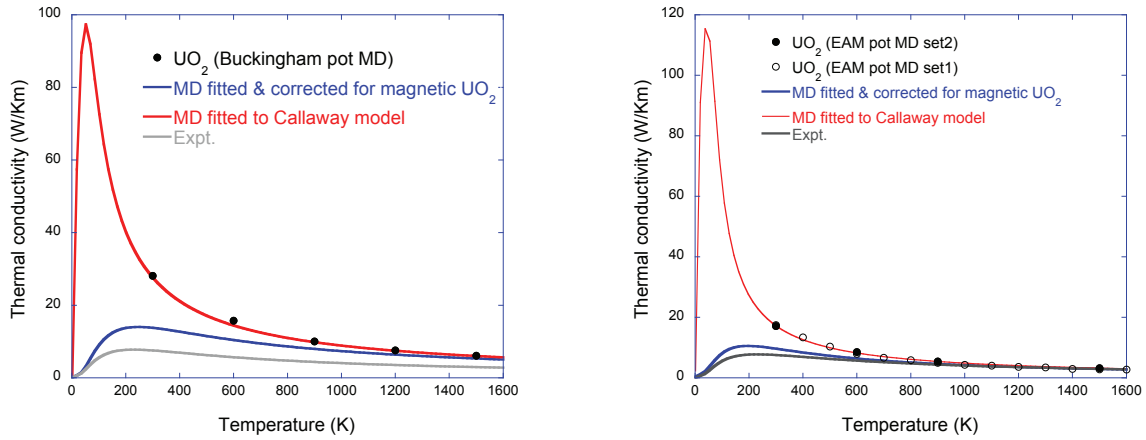

Figure 6: (a) MD simulation of the UO_2 thermal conductivity employing the Busker Buckingham potential, both with and without correction for spin-phonon scattering. The spin-phonon scattering correction was derived by fitting a Callaway model to the experimental data and then adding the spin-phonon relaxation time to the MD results. (b) Similar to (a) but emplying the EAM potential.

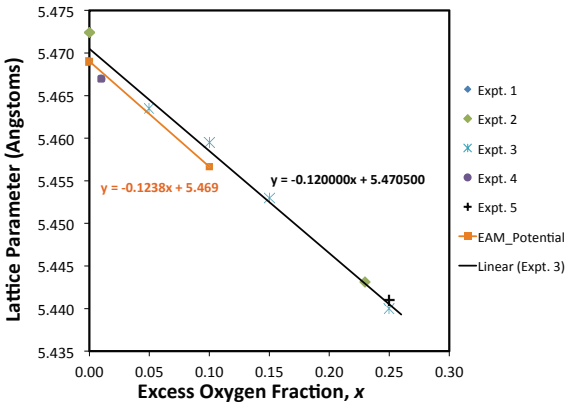

Figure 5: Lattice parameter of UO_{2+x} predicted by the new potential compared to available experimental data [53] .

In figure 6b, the MD results of thermal conductivities κ employing the EAM potential for pure UO_2 at different tempeatures are shown. Even for MD simulations employing the EAM potential, the κ values are substantially higher than the experimental values at low to intermediate temperatures. Again, the MD values are fitted to the Callaway model as shown in figure 6b. After the correction for the magnetic UO_2 contributions, the κ values are again greatly reduced, showing a good agreement with the experimental data.

The resultant parameters of non-magnetic version of the Callaway model fitted to the results of MD for pure UO_2 are reported in Table 6 for both empirical potentials. These parameters are combined with the experimentally determined spin scattering parameters in Table 1.

Despite the improvement achieved by including the experimental spin scattering components, the Busker potential remains significantly higher than the experimental values. This is particularly true in the high temperature Umklapp dominated region where magnetic effects are limited. This indicates that spin scattering is not sufficient to account for discrepancies between the potential and experiment. This may be due to the dependence of the longitudinal and transverse phonon group velocities (v_L and v_T) on the elastic constants [37]: $v_L = \sqrt{C_{11}/\rho}$ and $v_L = \sqrt{C_{44}/\rho}$. The Busker potential, as such, over-predicts phonon group velocity by over-predicting the C_{44} elastic constant (note that $C_{44} \rightarrow C_{12}$ if shells are omitted). Conversely, the EAM potential, which gives a much more accurate prediction of the single crystal elastic constants [19] is very close the experimental thermal conductivity once it has been adjusted to include magnetism. This indicates that the manybody potential provides a better description of the classical lattice.

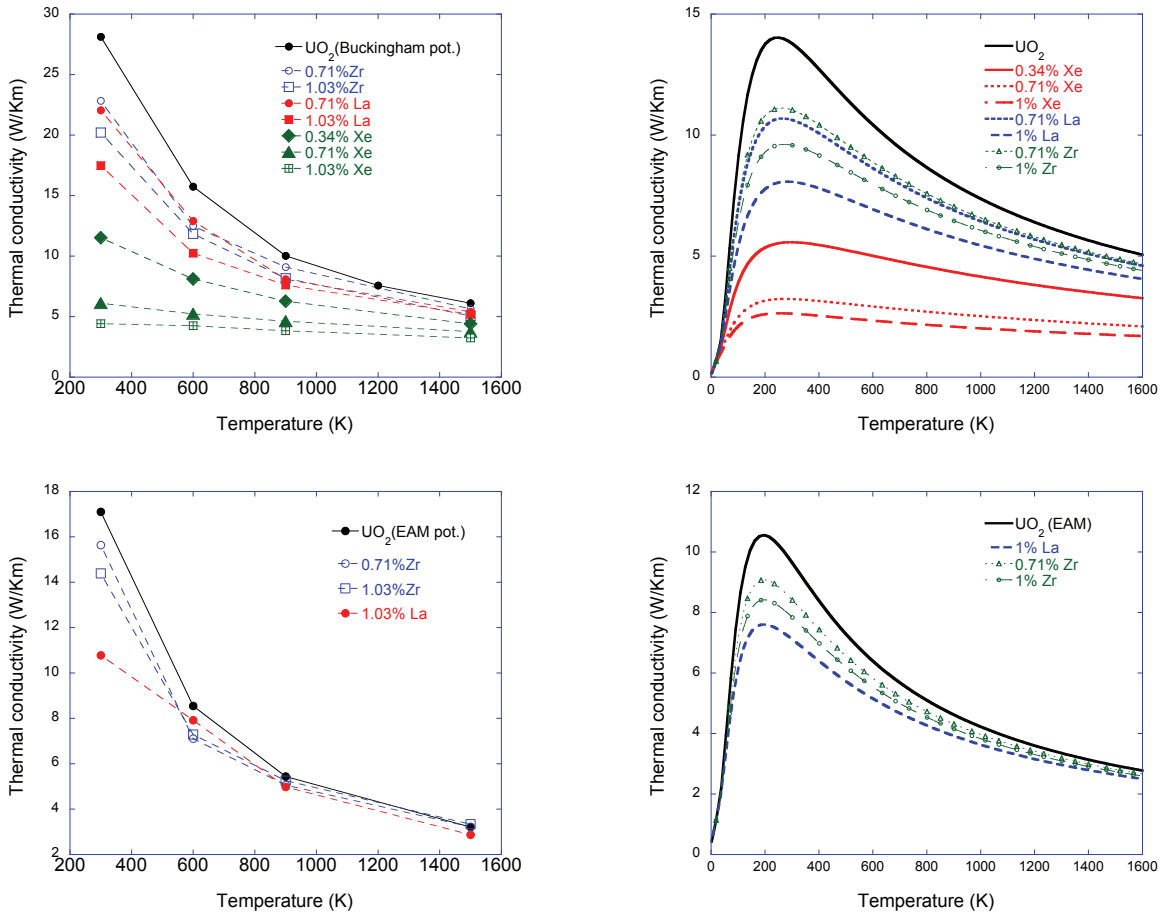

Figure 7: (a) κ for UO_2 at different temperatures of 0.71 and 1.03 atomic percent Zr, 0.71 and 1.03 atomic percent La, 0.34, 0.71, and 1.03 atomic percent Xe. κ for UO_2 at different temperatures obtained using the Buckingham potential is also plotted for comparison. (b) Reduction of UO_2 thermal conductivity by Xe, La, and Zr atoms, including correction for spin-phonon scattering. These results were obtained from the data in (a) by adding the spin-phonon scattering contribution derived from experimental data. (c) κ for UO_2 at different temperatures of 0.71 and 1.03 atomic percent Zr, and 1.03 atomic percent La employing the EAM potentials. κ for UO_2 at different temperatures obtained using the EAM potential is also plotted for comparison. (d) Reduction of UO_2 thermal conductivity by La, and Zr atoms, including correction for spin-phonon scattering. These results were obtained from the data in (c) by adding the spin-phonon scattering contribution derived from experimental data.

Table 6: Non-magnetic Callaway model parameters for pure UO_2 shown for both potentials.

Busker potential [18]			
D ($K^{-4}s^{-1}$)	B (s^{-1})	U ($K^{-3}s^{-1}$)	b
92.00518	2.174×10^8	20539.922	2.5535469
EAM potential [19]			
D ($K^{-4}s^{-1}$)	B (s^{-1})	U ($K^{-3}s^{-1}$)	b
154.85023	4.222×10^7	40912.969	1.8266757

5.2. Zr^{4+}, La^{3+} and Xe^0

MD simulations of the thermal conductivity of UO_2 containing the fission products Zr, La, and Xe were carried out. Zr and La, are substitute a single uranium cation, whereas Xe is accommodated at the bound Schottky defect. These are expected to be the energetically favourable incorporation sites for the respective fission products [54]. The locations of the substitution sites are chosen according to a random distribution for the specified composition. There is a charge imbalance of -1 when La^{3+} is introduced at a U^{4+} site, therefore for every La^{3+} one U^{5+} ion is randomly substituted at a U^{4+} site to ensure full charge compensation. The U^{5+} cations are distributed independently of the La^{3+} positions.

For MD simulations employing the Buckingham potentials, three compositions of fission products, 0.34, 0.71, and 1.03 atomic percent of Xe are introduced to the UO_2 samples. For Zr and La, the latter two compositions are used. In figure 7a the MD values for different concentrations of Zr, La, and Xe in UO_2 at different temperatures (300-1500 K) are shown. The sample lengths used to determine the values are 19 nm, 38 nm, and 57 nm for the Xe cases. Since the impurity scattering from the Xe Schottky defects is strong, the length dependence for all Xe cases is weak. For the Zr and La cases, since the impurity scattering from defects is much weaker, the length dependence is stronger, especially for cases with smaller La concentration. The sample lengths used to determine the κ values are similar to those in the Xe cases. The strong phonon scattering by the Xe Schottky defects severely reduces the thermal conductivity, even at the lowest concentration of 0.34 atomic percent. For example, at room temperature, the value changed from 28.1 W/Km to merely 11.5 W/Km in the 0.34% Xe case. Similar plots of κ for UO_2 with the fission product Zr and La suggest much weaker thermal scatterings. For example, also at room temperature, the value ranges from 22 to 17.5 W/Km for La concentrations from 0.71 to 1.03 atomic percent. These values are much higher than the Xe cases at the same temperature.

We can apply the same methodology to correct the MD predictions for UO_2 containing fission products (figure 7b). The general conclusions presented above for the impact on UO_2 thermal conductivity are still valid, but the overall conductivity is significantly reduced by including phonon-spin scattering, in particular at low temperatures. For all cases shown in figure 7b, as defect concentration increases, the thermal conductivity becomes smaller, indicating accumulative scattering effect to the thermal transport in UO_2. However, there is also some saturation effect for the scattering effect in the Xe cases in terms of concentration increase.

The MD simulations for the thermal conductivity of UO_2 containing fission products Zr and La employing the EAM potentials were carried out. The simulations of UO_2 containing Xe fission product were not carried out due to lack of interaction potentials. We are currently in the process of constructing such potential. For Zr, two compositions of fission products, 0.71 and 1.03 atomic percent are used. And for La, only the latter composition is used. In figure 7c, the MD values of thermal conductivities κ for different concentrations of Zr and La at different temperatures are shown. The results of corresponding magnetic corrections for the MD predictions are shown in figure 7d. Similar to the Buckingham potential results, the Zr fission product has weak thermal scattering at all temperatures examined. The result for La fission product shows modest reduction of the thermal conductivity at low temperatures.

5.3. Oxygen and uraniun point defects

For point defects, we considered oxygen interstitials (I_O), oxygen vacancies (V_O), uranium interstitials (I_U), and uranium vacancies (V_U). We also considered the Schottky trio vacancies, and compared the effect of Schottky defects to that of uranium vacancies. For the MD simulations employing the EAM potential, we considered only I_O and V_U defects since only U^{5+} charge model is available while U^{3+} charge model has not yet been developed, to combine with the current EAM model. I_O and V_U are also dominant species in most reacter fuel operation conditions. For each V_O or I_U defect, two or four U^{3+} ions are created in the supercell and randomly distributed in order to achieve charge compensation. Similarly, for each I_O or V_U

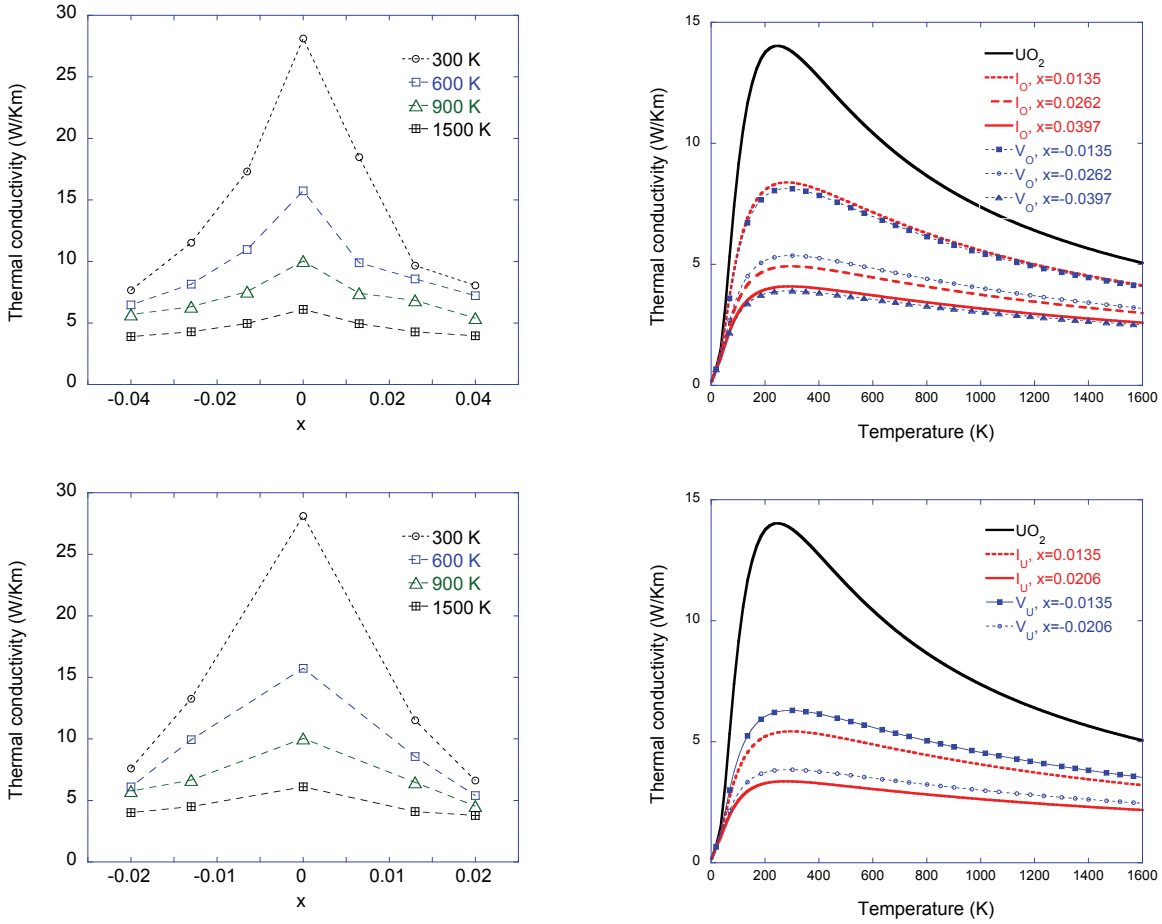

Figure 8: (a) The effect of I_O and V_O defects on the thermal conductivity of UO_2, as a function of x in UO_{2+x} at different temperatures. (b) Reduction of UO_2 thermal conductivity by oxygen defects, including correction for spin-phonon scattering. These results were obtained from the data in (a) by adding the spin-phonon scattering contribution derived from experimental data. (c) The effect of I_U and V_U defects on the thermal conductivity of UO_2, as a function of x in $U_{1+x}O_2$ at different temperatures. (d) Reduction of UO_2 thermal conductivity by oxygen defects, including correction for spin-phonon scattering. These results were obtained from the data in (c) by adding the spin-phonon scattering contribution derived from experimental data.

defect, two or four U^{5+} ions are created in the supercell and randomly distributed. The I_O position is in the center of the cubic UO_2 fluorite unit cell, as determined from DFT [54]. The I_U position is also in the center of the cubic UO_2 fluorite unit cell [54].

Figure 8a shows the effect of I_O and V_O on the thermal conductivity of UO_2, as a function of x in UO_{2+x} at different temperatures, employing the Buckingham potential. The results of corresponding magnetic corrections for the MD predictions are shown in figure 8b. Three compositions of oxygen defects, with x = 0.0135, 0.0262, and 0.0397, or 0.67, 1.31, 1.98 atomic percent of I_O (V_O) are introduced to the UO_2 samples. The impurity scattering from the oxygen defects is fairly strong, leading to a strong decrease in the thermal conductivity at modest temperatures (< 900 K), even for the smallest defect concentrations. The changes in thermal conductivity due to the I_O or V_O defects are approximately the same, suggesting that the impurity scatterings due to these two oxygen defects are similar. At higher temperatures, the reduction of thermal conductivity is smaller, but still shows a clear dependence on the defect concentrations.

Figure 8c shows the effect of I_U and V_U on the thermal conductivity of UO_2, as a function of x in $U_{1+x}O_2$ (the notation used to indicate uranium defects) at different temperatures, employing the Buckingham potential. The results of corresponding magnetic corrections for the MD predictions are shown in figure 8d. Two compositions of uranium defects, with x = 0.0135 and 0.0206, or 1.35 and 2.06 atomic percent of I_U (V_U) are introduced to the UO_2 samples. Both MD simulation temperatures and the sample lengths used to determine the thermal conductivity values are similar to the oxygen defect simulation cases. The impurity scattering from the uranium defects is stronger than the oxygen defect cases for the same x values. Although at the same x value, the concentration of the uranium defects is twice that of the oxygen defects, the total number of uranium defects is the same as that of the oxygen defects for the same simulation supercell, so the comparison for the same x value is still meaningful. The plot in Fig. 8c is slightly asymmetric around x = 0, reflecting that the scattering effect of I_U is slightly stronger (lower thermal conductivity) than that of V_U.

In figure 9a, the results of the EAM potential on the effects of I_O and V_U on the thermal conductivity of UO_2, as a function of x in UO_{2+x} (in I_O case) and $U_{1+x}O_2$ (in V_U case, x is negative) at different temperatures are shown. The results of corresponding magnetic corrections for the MD predictions are shown in figure 9b. Three compositions of oxygen defects, with x = 0.0135, 0.0262, and 0.0397 of I_O and two compositions of uranium defects, with x = 0.0135 and 0.0206 of V_U are introduced to the UO_2 samples. Consistent with the Buckingham potential results, as shown in figure 9, the impurity scattering from the uranium vacancies is stronger than the oxygen interstitials. At higher temperatures, the reduction of thermal conductivity is smaller, making the concentration dependence less distinguishable.

There are three types of Schottky trivacancy defects in UO_2: with two V_O aligned as nearest neighbors in [100] directions, or with two V_O aligned as next nearest neighbors in [110] directions, or a linear orientation of the O-U-O vacancies along [111] directions. We have chosen the Schottky trivacancy defect with two V_O aligned as next nearest neighbors in [110] directions since this defect configuration is one of the two lowest energy Schottky defect configurations [55–57] and is reported to be the most frequently observed of the three types of Schottky defects formed during displacement cascades [58]. There are two orientations of V_O pairs with respect to the heat flow direction, perpendicular to the direction or non-perpendicular. These two different orientations are named as V_{sch1} , and V_{sch2}. Figure 10 shows the comparison of the thermal conductivity of V_U and two different orientation configurations of Schottky trivacancy defects in UO_2, in two defect concentrations (x=0.013 and 0.02). From Fig. 10, it is suggested that there is no clear trend which configuration has more impurity scattering than the other. The difference among the thermal conductivities of these different configurations is generally small. In reality the orientation is probably random, but that does not matter if different orientations give rise to the similar scattering.

5.4. The Callaway defect scattering parameter D

The point defect scattering parameter D, fitted from the Callaway model is shown in this section. To unify the terms of concentration of different types of defects and impurities, the density of defects is used to define the concentration which is the number of defects divided by the total number of atoms in the otherwise perfect UO_2. Notice that this is different than "available site" fraction (C_s).

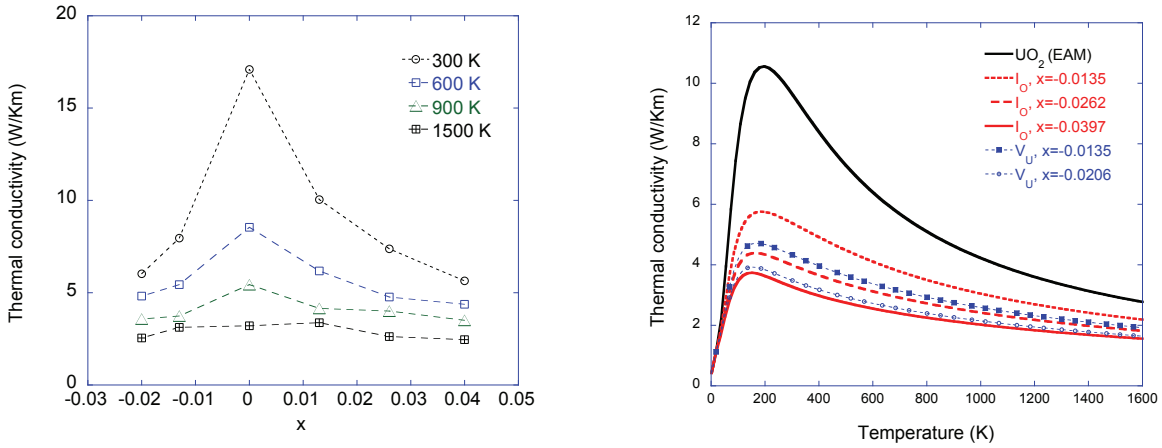

Figure 9: (a) The effect of I_O defects on the thermal conductivity of UO_2, as a function of x in UO_{2+x} at different temperatures, and the effect of V_U defects on the thermal conductivity of UO_2, as a function of x in $U_{1+x}O_2$ (negative x values) at different temperatures. All MD simulations were carried out employing the EAM potentials. (b) Reduction of UO_2 thermal conductivity by point defects, including correction for spin-phonon scattering. These results were obtained from the data in (a).

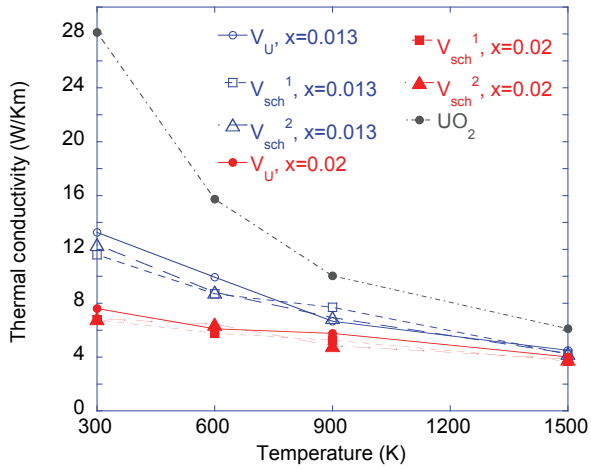

Figure 10: Comparison of the thermal conductivity of UO_2 with V_U defects and UO_2 with two different configurations of Schottky trivacancy defects (V_{sch1} , and V_{sch2}), as a function of temperature, for two defect concentrations (x=0.013 and 0.02). The thermal conductivity of bulk UO_2 is also plotted. The interatomic potential used in MD simulations is the Buckingham potential.

For example, in the V_U case, the density of defects concentration (C_d) equals one third of C_s, and in the V_O case, equals to two thirds of C_s.

In figure 11a, the D parameters of various fission products and point defects to the thermal conductivity of UO_2 employing the Buckingham potentials in MD simulations are shown. Consistent with MD results, it is shown that the fission products Zr^{4+} has smallest scattering effect on κ of UO_2, followed by La^{3+}. The highest D value is from fission product Xe occupying a Schottky trivacancy site. And the difference between the D values of Schottky trivacancy defect iself and Xe is modestly small. In addition, the differences of the D values among uranium interstitials, uranium vacancies, and Schottky trivacancies are also very small. In figure 11a, it is also shown that the the oxygen vacancies and interstitials share intermediate D values, with negligble differences, in good agreement with the trends in the MD simulation results.

The D values fitted from the MD simulations employing the EAM potentials are shown in figure 11b. From figure 11b, again, it is shown that the fission products Zr^{4+} has smallest scattering effect on the κ of UO_2, followed by La^{3+}. The oxygen interstitial has medium scattering effect, with magnitude in the D values in good agreement with the values from the Buckingham potential. The uranium vacancy has the highest D values , close to the Buckingham potential results. In general, both EAM and Buckingham potentials predict same trend and similar

values in the D values for point defects and fission products studied.

5.5. Charge compensation effect

Finally, we note the importance of including charge compensation in the MD simulations. This is especially true for V_U simulations where each vacancy defect is accommodated by four U^{5+} ions. In figure 11b, the D values of uranium vacancies *without* charge compensation is also shown, together with the D values of the isolated U^{5+} ions in different concentrations. While the D value of individual U^{5+} is small, approximately equal to that of Zr^{4+}, the accummulated effect of multiple U^{5+} can be significant. Indeed, without taking into account of the U^{5+} ions, the D values of uranium vacancies are in close proximity to that of oxygen interstitials (see figure 11b).

In irradiated UO_2 fuels, the charge state of point defects may also be charge uncompensated by U^{5+} or U^{3+} ions. This senario maybe in the case of Frenkel pairs, for example, where the intertstitial and vacancy defects are generated simultaneously. In such cases, the defects should be treated as charged species. The evaluation of charge compensation effect will help to assess the thermal scattering effect of both charge compensated and charged defects in UO_2 fuels.

5.6. Simple analytical expression

Many higher level fuel performance codes take expressions for defect scattering that are simpler than the Callaway model. These expressions are based on a proportional relationship between thermal conductivity and the effective phonon mean free path, $k \propto l_{eff}$. Furthermore, assuming a constant phonon group velocity and using Matthiessens's phonon relaxation rule one can express the separate contributions to the effective phonon mean free path as:

$$\frac{1}{l_{eff}} = \frac{1}{l_{defect}} + \frac{1}{l_{temp}} + \frac{1}{l_{misc.}} \qquad (11)$$

where l_{defect} and l_{temp} represent the phonon mean free path due to defect and Umpklapp scattering processes respectively. $l_{misc.}$ represents any other phonon scattering processes that remain, such as spin scattering. Thus, by fitting defect scattering (C), Umpklapp scattering (B) and miscellaneous scattering (A) parameters to the MD data the following expression can be derived for thermal conductivity:

$$k = \frac{1}{A + BT + Cx} \qquad (12)$$

where T is the temperature and x is the defect concentration, as defined previously. Note that for oxygen and uranium interstitials and vacancies x is taken to be the corresponding stoichiometry of $UO_{2\pm x}$. For fitting these parameters MD data above 500 K that has been corrected for spin scattering is used. A and B parameters are fitted to the pure UO_2 thermal conductivity as a function of temperature (blue curves in figure 6). Subsequently, A and B are fixed whilst C is adjusted for each defect species to reproduce the data reported in figures 7-9 above 500 K. The final parameter set for equation 12 is reported in Table 7.

Table 7: Parameters from equation 12 that were fitted to the spin corrected MD data, see figures 7-9, for defect scattering in UO_2 above 500 K.

	Busker	EAM
A (mKW^{-1})	3.46×10^{-2}	3.11×10^{-2}
B (mW^{-1})	1.01×10^{-4}	2.08×10^{-4}
C_{Xe} (mKW^{-1})	3.39×10^{-1}	-
C_{La} (mKW^{-1})	3.97×10^{-2}	3.75×10^{-2}
C_{Zr} (mKW^{-1})	2.23×10^{-2}	2.20×10^{-2}
$C_{U^{5+}}$ (mKW^{-1})	1.38×10^{-2}	1.99×10^{-2}
C_{U_i} (mKW^{-1})	9.80	-
C_{V_U} (mKW^{-1})	7.77	10.7
C_{O_i} (mKW^{-1})	4.28	6.42
C_{V_O} (mKW^{-1})	4.32	-

The difference in A and B between the Busker potential and the EAM potential is due to the disagreement between the two potentials in their description of the UO_2 lattice, as is clearly seen by figure 6. Particularly this is true for B which describes phonon-phonon interactions for which there is a factor of two difference between the potentials. Experimental $A = 0.115$ mKW^{-1} and $B = 2.48 \times 10^{-4}$ mW^{-1} values from Wiesenack *et al.* [59] show a good agreement with the EAM potential for the B term although additional temperature independent terms, such as defect scattering, may account for a larger A term. Nonetheless, despite the disagreement between the potentials on the pure UO_2 thermal conductivity there is a reasonable agreement for the defect scattering terms.

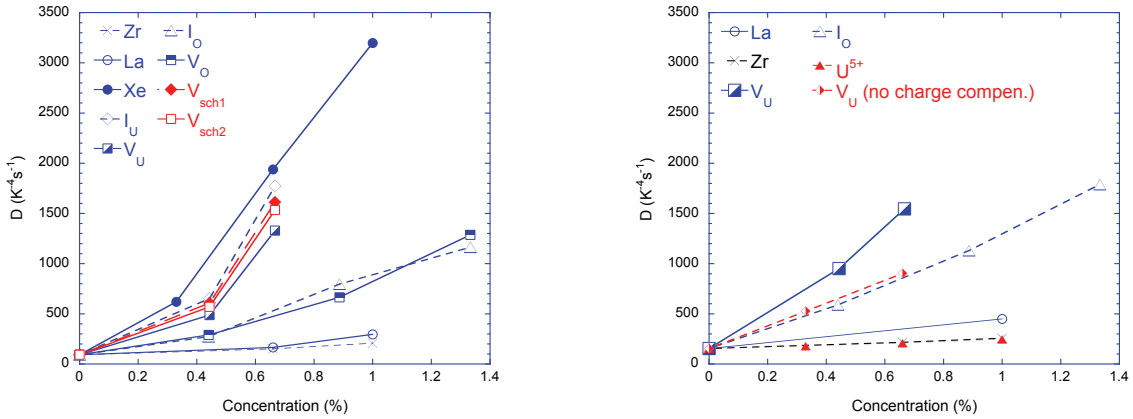

Figure 11: (a)The point defect scattering parameter D, fitted from the Callaway model of various fission products and point defects to the thermal conductivity of UO_2 employing the Busker Buckingham potential in MD simulations. (b) Same as in (a) but employing the EAM potential in MD simulations.

6. Experimental measurements of UO_2 and UO_{2+x} thermal conductivity

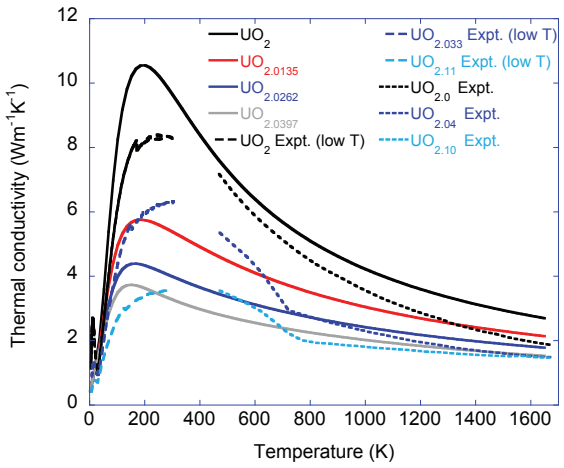

Figure 12: Comparison of the UO_{2+x} thermal conductivity obtained from MD simulations and from experiments. The high temperature experimental data were taken from White and Nelson [60] and the low temperature data are from the present study (UO_{2+x} or from Gofryk et al. [1] (UO_2). The low temperature experimental data were obtained by measurements on single crystals oriented in the [111] crystallographic direction.

The MD simulations for UO_{2+x} (corrected for resonant spin–phonon scattering) employing the EAM potential are compared to experimental measurements in figure 12. White and Nelson [60] reported the thermal conductivity for a range a UO_{2+x} stoichiometries at high temperature. Above $\sim$ 800 K the MD simulations overestimate the thermal conductivity, while it is underestimated below this temperature. The change in thermal conductivity with increasing oxygen content is correctly reproduced in each temperature range. One complication in comparing the MD and experimental results is the strong tendency of UO_{2+x} to phase separate into UO_2+U_4O_9. The transition to a single UO_{2+x} phase occurs at $\sim$800 K and is responsible for the kink in the experimental thermal conductivity measurements. The mixed UO_2+U_4O_9 phase has much higher thermal conductivity than the corresponding disordered UO_{2+x} phase, which is understood in terms of the increased point defect scattering in UO_{2+x} compared to UO_2. U_4O_9 has very low thermal conductivity. The MD simulations model a perfectly disordered UO_{2+x}, which is only relevant well above 800 K. The UO_2+U_4O_9 phase separation explains why the MD thermal conductivity is lower than the experimental results below 800 K. In agreement with the results for stoichiometric UO_2, the MD simulations seem to slightly overestimate the thermal conductivity above 800 K even after correcting for spin–phonon scattering. We believe that this is a consequence of the empirical potential employed in this study. In this context, note that the overestimation is very similar in magnitude to the comparison between theory and experiments for stoichiometric UO_2. Consequently, this discrepancy may be inherited from the empirical potential description of UO_2 rather than from the scattering

properties of interstitial oxygen ions.

7. Summary

In summary, the thermal transport in UO_2 with defects and fission products has been investigated using non-equilibrium MD simulations. Two sets of empirical potentials are used as basis for studying the degregation of UO_2 thermal conductivity due to defects and fission products including a Buckingham type and a recently developed EAM type potentials. New parameter sets for the U^{5+} and Zr^{4+} are developed for the EAM potential. The thermal conductivity results from the MD simulations are then fitted to the classical Callaway model. Combined with the magnetic terms derived from very low temperature experiments, the corrected Callaway model parameters for the pure UO_2 and UO_2 with defective structures are obtained, to predict the degradation of UO_2 thermal conductivity with defects. Finally, to validate the modelling results, comparison was made with experimental measurements on single crystal hyper-stoichiometric UO_{2+x} samples.

Acknowledgements

We thank Michael R. Tonks at INL and Blas P. Uberuaga at LANL for helpful suggestions. This work was funded by the Department of Energy Nuclear Energy Advanced Modeling and Simulation program.

[1] K. Gofryk, S. Du, C. Stanek, J. Lashley, X.-Y. Liu, R. Schulze, J. Smith, D. Safarik, D. Byler, K. McClellan, B. Uberuaga, B. Scott, D. Andersson, Nat. Commun. 5 (2014) 4551.
[2] M. Amaya, M. Hirai, H. Sakurai, K. Ito, M. Sasaki, T. Nomata, K. Kamimura, R. Iwasaki, J. Nucl. Mater. 300 (2002) 57–64.
[3] Thermophysical Properties Database of Matertials for Light Water Reators and Heavy Water Reactors, Technical Report IAEA-TECDOC-1496, International Atomic Energy Agency, 2006.
[4] T. Watanabe, S. Sinnott, J. Tulenko, R. Grimes, P. Schelling, S. Phillpot, J. Nucl. Mater. 375 (2008) 388–396.
[5] T. Uchida, T. Sunaoshi, M. Kato, K. Konashi, Prog. Nucl. Sci. Tech. 2 (2011) 598–602.
[6] A. Chernatynskiy, C. Flint, S. Sinnott, S. Phillpot, J. Mater. Sci. 47 (2012) 7693–7702.
[7] S. Yamasaki, T. Arima, K. Idemitsu, Y. Inagaki, Int. J. Thermophys. 28 (2007) 661–673.
[8] T. Watanabe, S. Srivilliputhur, P. Schelling, J. Tulenko, S. Sinnott, S. Phillpot, J. Am. Ceram. Soc. 92 (2009) 850–856.
[9] S. Nichenko, D. Staicu, J. Nucl. Mater. 433 (2013) 297–304.
[10] M. Tonks, P. Millett, P. Nerikar, S. Du, D. Andersson, C. Stanek, D. Gaston, D. Andrs, R. Williamson, J. Nucl. Mater. 440 (2013) 193–200.
[11] P. S. B. Deng, A. Chernatynskiy, R. Stoller, S. Sinnott, S. Phillpot, J. Nucl. Mater. 434 (2013) 203–209.
[12] C.-W. Lee, A. Chernatynskiy, P. Shukla, R. Stoller, S. Sinnott, S. Phillpot, J. Nucl. Mater. 456 (2015) 253–259.
[13] M. Cooper, S. Middleburgh, R. Grimes, J. Nucl. Mater. 466 (2015) 29–35.
[14] T. Arima, S. Yamasaki, Y. Inagaki, K. Idemitsu, J. Alloys Compd. 415 (2006) 43–50.
[15] J.-J. Ma, J. Zheng, M.-J. Wan, J.-G. Du, J. Yang, G. Jiang, J. Nucl. Mater. 432 (2006) 230–234.
[16] S. L. Dudarev, P. M. Derlet, J. Phys.: Condens. Matter 17 (2005) 7097–7118.
[17] R. A. Buckingham, Proc. Roy. Soc. Lond. Ser. A Math. Phys. Sci. 168 (1938) 264–283.
[18] G. Busker, A. Chroneos, R. Grimes, I. Chen, J. Am. Ceram. Soc. 82 (1999) 1553–1559.
[19] M. Cooper, M. Rushton, R. Grimes, J. Phys. Condens. Matter. 26 (2014) 105401.
[20] M. S. Daw, M. I. Baskes, Phys. Rev. B 29 (1984) 6443–6453.
[21] P. M. Morse, Phys. Rev. B 34 (1929) 57–64.
[22] M. Tonks, D. Gaston, P. Millett, D. Andrs, P. Talbot, Comp. Mat. Sci. 51 (2012) 20–29.
[23] P. Jund, R. Jullien, Phys. Rev. B 59 (1999) 13707–13711.
[24] F. MullerPlathe, J. Chem. Phys. 106 (1997) 6082–6085.
[25] T. Ikeshoji, B. Hafskjold, Mol. Phys. 81 (1994) 251–261.
[26] X. Zhou, S. Aubry, R. Jones, A. Greenstein, P. Schelling, Phys. Rev. B 79 (2009) 115201.
[27] S. Plimpton, J. Comp. Phys 117 (1995) 1–19.
[28] P. Howell, J. Comput. Theor. Nanos. 8 (2011) 2129–2143.
[29] R. W. Grimes, J. Am. Ceram. Soc. 82 (1999) 1553–1559.
[30] R. W. Grimes, C. R. A. Catlow, Phil. Trans. R. Soc. Lond. A 335 (1991) 609–634.
[31] R. G. J. Ball, R. W. Grimes, J. Chem. Soc., Faraday Trans. 86 (1990) 1257–1261.
[32] L. Minervini, Atomistic Simulations of Defective Oxides, Ph.D. thesis, Imperial College (2000).
[33] R. Cleave, Atomic Scale Simulations for Waste Form Applications, Ph.D. thesis, Imperial College (2000).
[34] B. E. Hanken, C. R. Stanek, N. Grønbech-Jensen, M. Asta, Phys. Rev. B 84 (2011) 085131. doi:10.1103/PhysRevB.84.085131.
[35] D. Wolf, P. Keblinski, S. Phillpot, J. Eggebrecht, J. Chem. Phys. 110 (1999) 8254–8282.
[36] J. Callaway, Phys. Rev. 113 (1959) 1046–1051.
[37] P. Schelling, S. Phillpot, D. Wolf, J. Am. Ceram. Soc. 84 (2001) 1609–1619.
[38] B. Bondars, G. Heidemane, J. Grabis, K. Laschke, H. Boysen, J. Schneider, F. Frey, J. Mater. Sci. 30 (1995) 1621.
[39] P. Aldebert, J.-P. Traverse, J. Am. Ceram. Soc. 68 (1985) 34.
[40] G. Teufer, Acta Cryst. 15 (1962) 1187.
[41] J. D. Gale, J. Chem. Soc. 93 (1997) 629.
[42] M. W. D. Cooper, S. T. Murphy, P. C. M. Fossati, M. J. D. Rushton, R. W. Grimes, Proc. Roy. Soc. Lond. A 470 (2014) 20140427.

[43] R. D. Shannon, Acta Crystallogr. A (1976) 751.
[44] E. H. Kisi, C. J. Howard, J. Am. Ceram. Soc. 84 (1998) 1682.
[45] G. Fadda, L. Colombo, G. Zanzotto, Phys. Rev. B 79 (2009) 214102.
[46] Y. Natanzon, M. Boniecki, Z. Lodziana, J. Phys. Chem. Solids 70 (2009) 15–19.
[47] J. E. Lowther, Phys. Rev. B 73 (2006) 134110.
[48] V. Milman, A. Perlov, K. Refson, S. J. Clark, J. Gavartin, D. Winkler, J. Phys. Condens. Matter 21 (2009) 485404.
[49] P. Bouvier, E. Djurado, G. Lucazeau, T. Le Bihan, Phys. Rev. B 62 (2000) 8731.
[50] C. J. Howard, R. J. Hill, B. E. Reichert, Struct. Sci 44 (1988) 116.
[51] H. G. Scott, J. Mater. Sci. 10 (1975) 1527.
[52] D. A. Andersson, G. Baldinozzi, L. Desgranges, D. R. Conradson, S. D. Conradson, Inorg. Chem. 52 (2013) 2769–2778.
[53] S. Middlebourgh, private communications (2015).
[54] X.-Y. Liu, D. Andersson, B. Uberuaga, J. Mater. Sci. 47 (2012) 7367–7384.
[55] B. Dorado, M. Freyss, G. Martin, Europ. Phys. J. B 69 (2009) 203–209.
[56] A. E. Thompson, C. Wolverton, Phys. Rev. B 84 (2011) 134111. doi:10.1103/PhysRevB.84.134111.
[57] X.-Y. Liu, D. Andersson, J. Nucl. Mater. 462 (2015) 8–14.
[58] G. Martin, P. Garcia, C. Sabathier, L. V. Brutzel, B. Dorado, F. Garrido, S. Maillard, Phys. Lett. A 374 (2010) 3038–3041.
[59] W. Wiesenack, IAEA Tech. Comm. Meeting on Fission Gas Release and Fuel Rod Chemistry Related to Extended Burnup, IAEA-TECDOC-697, 27 April-1 May 1992, Pembroke, Canada (April 1993).
[60] T. White, N. A. T., J. Nucl. Mater. 443 (2013) 342.